

Atomic resolution imaging of 3D crystallography in functional oxide thin films

Ian MacLaren¹, Aurys Silinga¹, Juri Barthel², Josee Kleibeuker^{3,4}, Judith L MacManus-Driscoll³, Christopher S Allen^{5,6}, Angus I Kirkland^{5,6}

1. School of Physics and Astronomy, University of Glasgow, Glasgow G12 8QQ, UK
2. Ernst Ruska-Centre (ER-C 2), Forschungszentrum Jülich GmbH, 52425 Jülich, Germany
3. Department of Materials Science & Metallurgy, University of Cambridge, 27 Charles Babbage Road, Cambridge CB3 0FS, UK
4. DEMCON high tech systems Eindhoven BV, Kanaaldijk 29, 5683 CR Best, The Netherlands
5. electron Physical Science Imaging Centre, Diamond Light Source Ltd., OX11 0DE, UK
6. Department of Materials, University of Oxford, Parks Road, Oxford OX1 3PH, UK

Whilst atomic resolution imaging in the scanning transmission electron microscope (STEM) has revolutionized science and technology, it cannot see things happening out of the plane of the image and merely forms projection images. In this article we show that it is possible to directly map the direction and magnitude of atom displacements at 30° to the imaging plane in a $\text{La}_2\text{CoMnO}_6$ thin film on (111) LSAT (LaAlO_3 - $(\text{Sr,Ta})\text{AlO}_3$) using a 4-dimensional scanning transmission electron microscopy (4DSTEM) methodology. The interpretation is backed up by analysis of theoretical simulations. We reveal that the b-axis always lies in the plane of interface in every area we looked at, and that the atom modulation is strongly suppressed close to the epitaxial interface. This crystallographic detail was not previously revealed or visible by conventional STEM imaging and the new methodology sheds a lot more light on why this particular substrate in this orientation best promotes double perovskite cation ordering and consequently the best achieved magnetic ordering in this thin film system. This approach of fitting atomic resolution 4DSTEM data to determine crystal parameters opens the door for a new era of atomic-resolution crystallography.

Introduction

Atomic resolution imaging in the scanning transmission electron microscope (STEM) has revolutionised science and technology, especially since the introduction of aberration correction^[1-2], making sub-Ångström resolution easily realised. The ability to simply see two-dimensional projections of the atomic structure in thin specimens of crystalline solids

has allowed unprecedented understanding of local features in nanostructures, such as interfaces, as well as of defects within materials and heterostructures^[3-5]. In specific cases, more information about the 3-dimensional structure can be determined by looking at multiple examples of the same structure using discrete tomography^[6-8], or from conventional tilt-tomography, although the latter is hard to perform at atomic resolution^[9] at reasonable fluence levels. Recently, however, major advances have been made in STEM with the advent of fast-readout direct electron detectors for 4DSTEM^[10-11], which offers possibilities for novel imaging modalities not possible with monolithic annular^[12-14], circular^[15] or segmented detectors^[16-17]. We have previously shown that high angle electron diffraction into higher-order Laue zones produces an atomic resolution signal^[18], which reveals information about the 3D order in a crystal. This current work goes far beyond that and shows that the atomic resolution diffraction data contains information about the exact 3D orientation of one unique axis of the unit cell and the magnitudes of atom movements along it; and that this can be mapped at atomic resolution by fitting a simple mathematical model. In short, we show that by measuring and fitting high angle scattering, 4DSTEM can perform atomic resolution imaging of 3D crystal ordering without any need for sample tilting. Such approaches will provide a major step forward in understanding the details of nanoscale heterostructures, including surface reconstructions and interface structures.

Characterising the local crystallographic structure of materials is key to understanding their behaviour and how the growth or fabrication leads to a given structure with specific properties. However, despite the ability of electron microscopy to image nanostructures with atomic resolution, this remains a two-dimensional projection and gaining access to information in the third dimension is very challenging in dimensionally constrained samples such as few-nm thin films or domain structures. Such considerations are especially pertinent when considering the optimisation of functional oxides and other functional materials, which are often grown as epitaxial systems with interfaces exerting a significant control over the resulting structure, chemical ordering and properties, particularly through strain transfer. However, we previously demonstrated that some information about the periodicity in the third dimension was available using a *HOLZ-STEM* (higher-order Laue zone - scanning transmission electron microscopy) approach^[19], and that this is atomically resolved^[18] (as also shown without 4DSTEM by Huang *et al.*^[20]). This only recently became convenient to perform because of the advent of 4DSTEM (4-dimensional scanning transmission electron microscopy) in which a scan is performed over an area with a diffraction pattern recorded to a suitably fast detector at every scan point^[10-11]. Nevertheless, more directional information than this about atomic displacements was absent until now.

Antiparallel atom displacements in perovskites

A common feature of functional oxides is octahedral coordination of the smaller cations and the coordinated tilting of these octahedra, often coupled with antiparallel displacements of the larger cations²¹. Whilst octahedral tilting is particularly common in perovskites and there exists a specific classification scheme for the tilting patterns thereof²², similar effects are observed in a much wider range of functional oxides. This is particularly likely where the unit cell contains more than one similar layer and the cation is located away from a centrosymmetric position, as is seen, for example, in some tungsten bronzes²³. Figure 1 shows a side view of a one-atom-thick slice of the structure of $\text{La}_2\text{CoMnO}_6$ (LCMO), as refined by Bull *et al.*²⁴ (although with displacements exaggerated to make them clearer to

the reader), showing such antiparallel displacements of alternate La atoms along the $[111]$ direction, the majority of modulus of the displacement being along the \mathbf{b} direction (actually $\mathbf{d} = \pm 0.057[1, 3.80, \overline{1.08}]$). A key point is that rotating the crystal by 180° about the beam direction ($[111]$ in the figure) does not result in equivalent 3D structures, one showing an up-left, down-right pattern, and the other an up-right, down-left pattern. Despite this clear difference in 3D structure, projection images of any sort (such as annular dark field STEM) taken along $[111]$ from crystals represented by the two panes of Figure 1 would be identical. A 3D view of these coordinated atom movements and how they relate the sample overall (e.g., at interfaces and strain fields) would be invaluable in better understanding the growth of complex oxides, especially in the presence of interfaces and/or multiple domains on the nanoscale. Either of these would make tilt tomography approaches impracticable. This would in turn inform the optimisation of the growth to produce atomic structures with the desired properties.

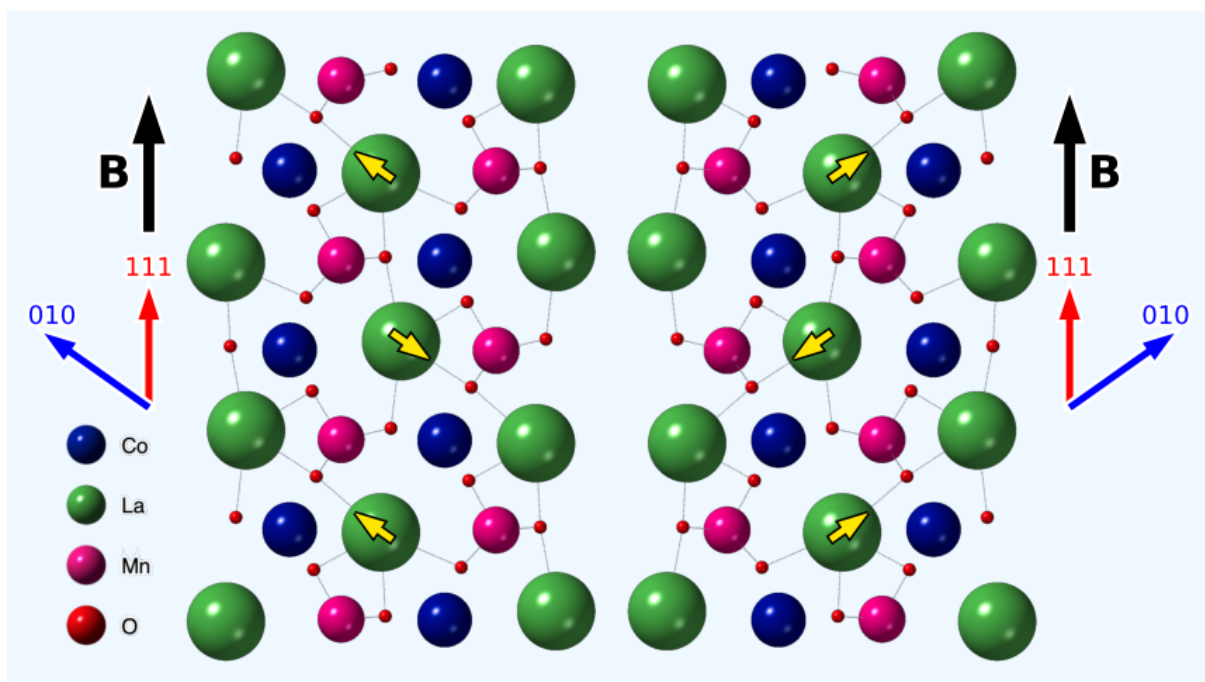


Figure 1: schematic view of columns of atoms along the $[111]$ direction (vertical) in $\text{La}_2\text{CoMnO}_6$ in which there are alternate antiparallel La cation displacements along a direction close to $[001]$. Two possible orientations of the crystal are shown, containing the same vertical $[111]$ direction, but differing by a 180° rotation about this vertical direction). These two crystal orientations would give indistinguishable projection images when recorded with a beam direction parallel to $[111]$ (i.e. the 2D projection symmetry includes a 2-fold rotation), however the 3D orientation of the \mathbf{b} axis is switched. Just one plane of the crystal is shown for simplicity. La atom displacements are magnified by a factor of 3 to aid visualisation.

Fitting the azimuthal diffracted intensity variation at atomic resolution

We showed recently that unidirectional atom position modulations as shown in Figure 1 lead to a strong periodic azimuthal intensity variation in the First-Order Laue Zone (FOLZ) ring clearly aligned with the modulation direction. It was shown that this can be used to

determine the modulation direction and strength through fitting the azimuthal variation to a simple periodic function²⁵, in a way that is far more accurate and informative than simple atomic resolution imaging. However, this was just performed on larger image patches covering several unit cells and no attempt was made to do so at atomic resolution, or to investigate the details of what might emerge from such fitting at atomic resolution. Figure 2b) shows a representative diffraction pattern averaged over a significant image area (to improve signal to noise) with the FOLZ indicated within dotted lines describing two concentric circles. The data was polar transformed and could then be integrated to a single intensity plot as a function of azimuthal angle (measured anticlockwise from horizontal-right). This was then fitted with the fit function described in our previous work as:

$$I(\theta) = A_2 \cos^2(\phi - \phi_2) + A_1 \cos(\phi - \phi_1) + B \quad [1]$$

The fit shown in Figure 2a clearly peaks close to 90° and 270°, with additional intensity on the 90° side (top of diffraction pattern).

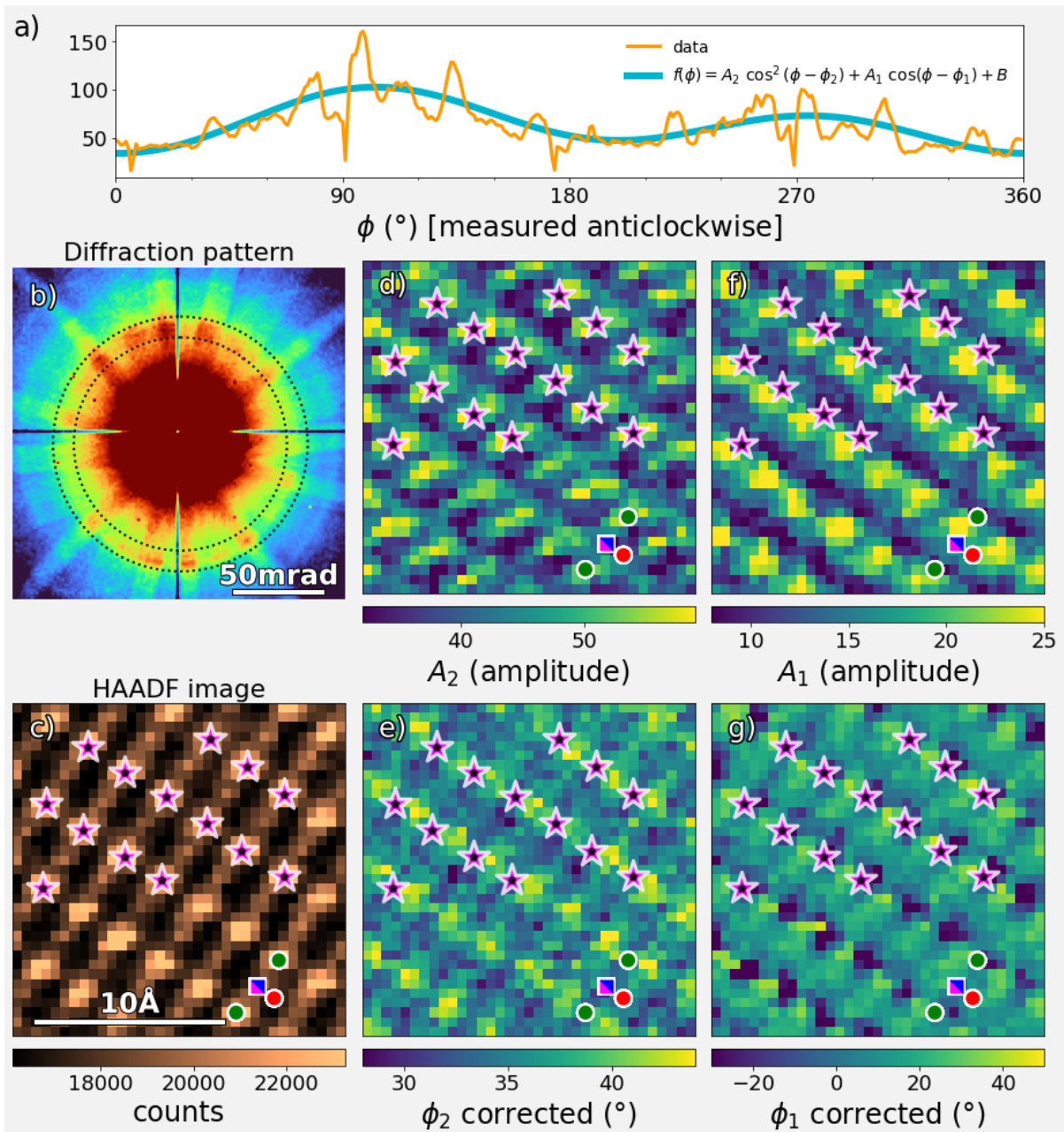


Figure 2: Atomic resolution fitting of the First Order Laue Zone ring in a region of a $\text{La}_2\text{CoMnO}_6$ film calculated from a 4DSTEM dataset recorded along a $\langle 111 \rangle_{\text{monoclinic}}$ direction. This shows b) a sum diffraction pattern from the whole area with the FOLZ ring indicated with dotted lines; a) the fit of the ring from this sum pattern after polar transformation; c) a HAADF image calculated from the dataset for angles $>79\text{mrad}$; and d), e), f) and g) fit maps for the parameters A_2 , ϕ_2 , A_1 and ϕ_1 as defined in equation 1 and the legend of part b). An overlay of La-O atomic column positions is given on maps c)-g), together with a unit cell key (green – La-O, magenta/blue – manganese/cobalt, red – O).

The remainder of Figure 2 shows the results of applying this approach to every pixel of an atomic resolution 4DSTEM scan of a single crystal area of a $\text{La}_2\text{CoMnO}_6$ thin film (grown on $\text{LaAlO}_3\text{-(Sr,Ta)AlO}_3\text{-LSAT}$)²⁶. A HAADF image was calculated from the polar transformed data by simply integrating all intensity above a scattering angle of 79 mrad and this shows the

expected appearance for a perovskite viewed along a $\langle 110 \rangle_{\text{cubic}}$ direction. The centres of the brightest peaks in the upper half of the image (as determined using Gaussian interpolation), arising from La-O columns, are indicated by fuchsia stars, and these stars are overlaid on the equivalent images from the FOLZ fitting. Figure 2d-g) show best fitting A_2 , ϕ_2 , A_1 and ϕ_1 parameters of equation (1) where A_2 is the amplitude of the 2-fold intensity modulation, ϕ_2 is the peak angle of that 2-fold modulation (defined in the range 0-180°), A_1 is the amplitude of the 1-fold intensity modulation, and ϕ_1 is the phase of that 1-fold modulation (defined in the range 0-360°). B is not shown as it is just the offset of the base level of the FOLZ from zero, which is mainly a function of specimen thickness/density and is rather similar in form to the HAADF image. The first overarching point is that all these parameter maps are very consistent and show clear repeating patterns across each unit cell which do not simply mirror the HAADF intensity and clearly contain information absent from the projection-only HAADF image. Thus, mapping diffraction features, whatever the precise interpretation thereof, reveals things never previously seen in atomic resolution STEM imaging. For specific parameters, the A_2 map shows an unexpected feature where the strength of the 2-fold oscillation does not peak at the position of the atom columns in the HAADF image but appears elongated either side of the atom column centre, and is small elsewhere. The ϕ_2 map (corrected in angle as clockwise from the normal to $[1\bar{1}0]$, assuming the beam direction is $[111]^*$) is centred at around 35°, as expected²⁵, although this angle twists near the La-O column positions and around the A_2 peaks: to the lower right of each La-O column it peaks up to about 41-42° and in-between the La atom rows, it dips to below 35°. The A_1 map of the unidirectional intensity modulation is particularly surprising as it peaks away from the La column centres, towards one of the arms of the A_2 -elongated peak. On the other side of the same La-O column, it shows a large dip in intensity. Finally, the peak angle for the unidirectional distortion measured by the ϕ_2 parameter is approximately constant over most of the image but shows significant variations near the dips in the A_1 parameter (with very large uncertainties because it is poorly defined when the unidirectional modulation is weak).

Atomic resolution diffracted intensity shows the atom displacements

To interpret the atomic resolution detail in diffraction pattern fitting, multislice simulations^{27,28} were performed for a suitable supercell of the structure followed by application of the same polar transformation and fitting as used on the experimental data. This is shown in the upper part of Figure 3, where HAADF intensity, and the A_2 , ϕ_2 and A_1 parameters are plotted. For ease of comparison with experimental data, a patch of the same experimental dataset as used to make Figure 2 was processed as before and the results then interpolated by a factor of 4 to allow subpixel alignment. Image patches around 121 different La-columns were then superimposed and averaged to make representative supercell images of each parameter. The visual comparison is evident and, whilst the

* There are a number of directions in the orthorhombic/monoclinic structure which all give similar patterns equivalent to $\langle 1\bar{1}0 \rangle$ in primitive perovskite with a similar 2-fold modulation of the azimuthal intensity in an extra Laue zone ring. These are $[111]$, $[1\bar{1}1]$, $[11\bar{1}]$ and $[1\bar{1}\bar{1}]$, together with the negatives of these directions. More about simulations of different directions of this type is shown in the Supplemental Information.

simulations have slightly stronger contrast and better spatial resolution, it is clear that the theory and experiment are mostly in good agreement. This then allows the possibility of interpreting those experimental images in terms of crystallographic parameters. One thing to note is the asymmetric dip and peak in A_1 magnitude is reproduced in theory for a perfectly aligned beam along the axis. This shows that the A_1 parameter is not merely due to mistilt, as we erroneously assumed previously²⁵. It is also clear in this figure that the A_2 parameter map shows dumbbell-like structures peaked to either side of the column centre observed in the HAADF image.

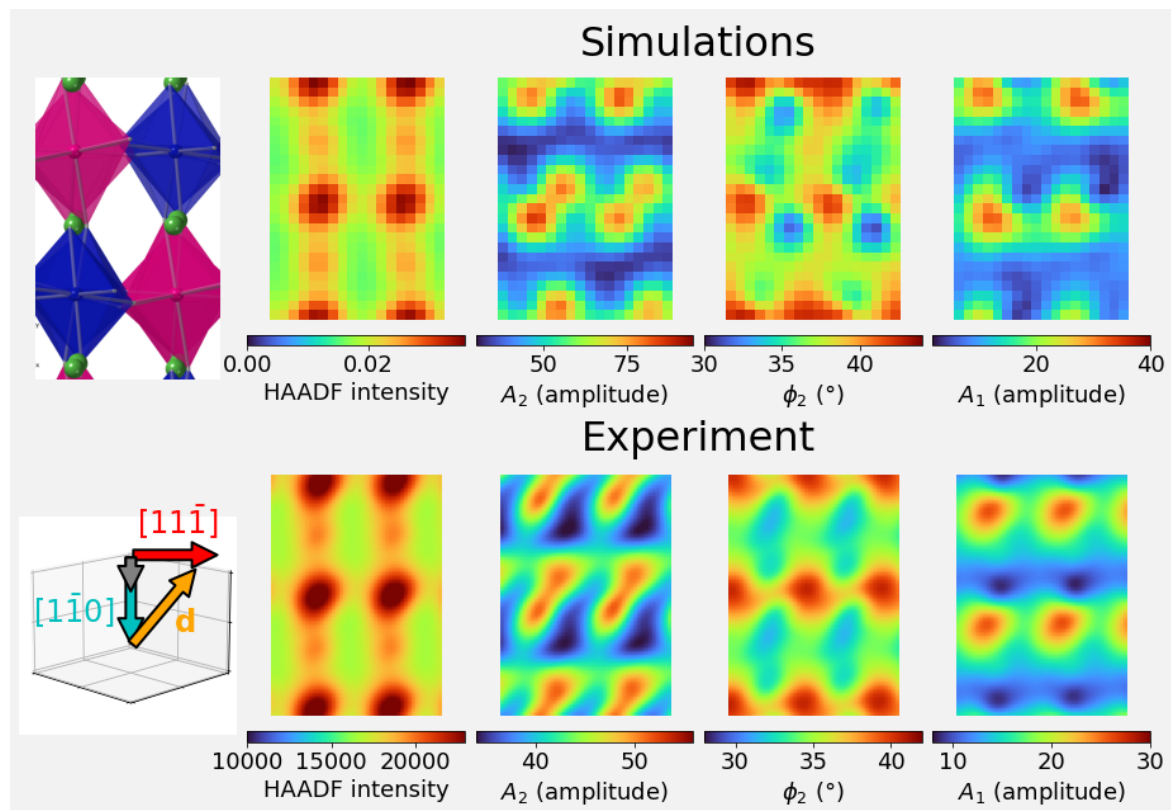


Figure 3: Comparison of azimuthal fitting applied to simulated 4DSTEM datasets compared to template averaging of experimental fits from the part of the same dataset as shown in Figure 2 (after upsampling by a factor of 4 before alignment to aid registration with $\frac{1}{4}$ pixel accuracy). Insets show a schematic diagram of the crystal structure in this projection (atom colours as for Figures 1 and 2) and a 3D plot of specific crystal directions in this figure (the orange arrow for \mathbf{d} is pointing up, right and towards the reader), the grey arrow is the beam direction.

The calculation shown is for a $[111]$ beam direction (i.e. the direction pointing upwards, antiparallel to the direction of electron motion and parallel to the direction of current flow), with the $[010]$ direction pointing to the upper right and up out of the page. This is in the direction from the A_1 peak to the A_1 dip for each La-O column, or alternately from the A_1 peak to the nearby HAADF peak. This then provides an unambiguous method for determining the 3D orientation of the La displacement direction (\mathbf{d} -direction) (refer to supplemental materials for a demonstration that the same applies for other $\langle 111 \rangle$ type directions in this crystal structure). It is already known that the strength of the FOLZ is approximately linearly dependent on the magnitude of atom position modulations along this

d-direction¹⁹. Thus, by combining these the HAADF, A_2 , ϕ_2 and A_1 maps, we can get the i) strength of the modulations (from A_2), ii) the direction of the modulations (and therefore the direction of the **d**-direction with a 180° ambiguity) (from the ϕ_2 parameter measured at the peak positions of the ϕ_1 parameter) and iii) the absolute sense of the direction in which the **d**-vector is pointing up out of the page (from where the peaks of the A_1 parameter lie with respect to the peak of the HAADF intensity).

Mapping atomic displacements in 3D across an interface

From the above, we have determined these parameters from a set of HAADF, A_2 , ϕ_2 and A_1 maps. In Figure 4, this is shown for a 4DSTEM scan across an area containing an interface between a LSAT substrate (top left) and a LCMO thin film. Using the procedure outlined above, Figure 4 shows arrows (aka a quiver plot), whose angles represent the directions of the **d**-vector for each atomic column, whose heads point in the direction in which the **d**-vector has a positive inclination (i.e. upwards from the plane of the page, so an up-right, down-left displacement pattern would give a right pointing arrow and an up-left, down-right displacement pattern would give a left pointing arrow), and whose length corresponds to the strength of the atom modulation along this direction. Additionally, the arrows are coloured according to the *HSV* colour wheel superimposed, where *Hue* represents the angle of the **d**-direction in the plane, and *Saturation* represents the strength of the modulation, and *Value* is set to 1. This map is superimposed on a semi-transparent version of the HAADF image as a guide to the eyes. The HAADF image shows the characteristic contrast of LSAT (above the interface) along $\langle 110 \rangle_{cubic}$ where different patches show slightly different ordering because of internal chemical inhomogeneity. The LCMO (below the interface) shows the typical appearance for a simple perovskite along this beam direction (as also shown in Figure 2 for the HAADF intensity) with little obvious sign of atomic modulation.

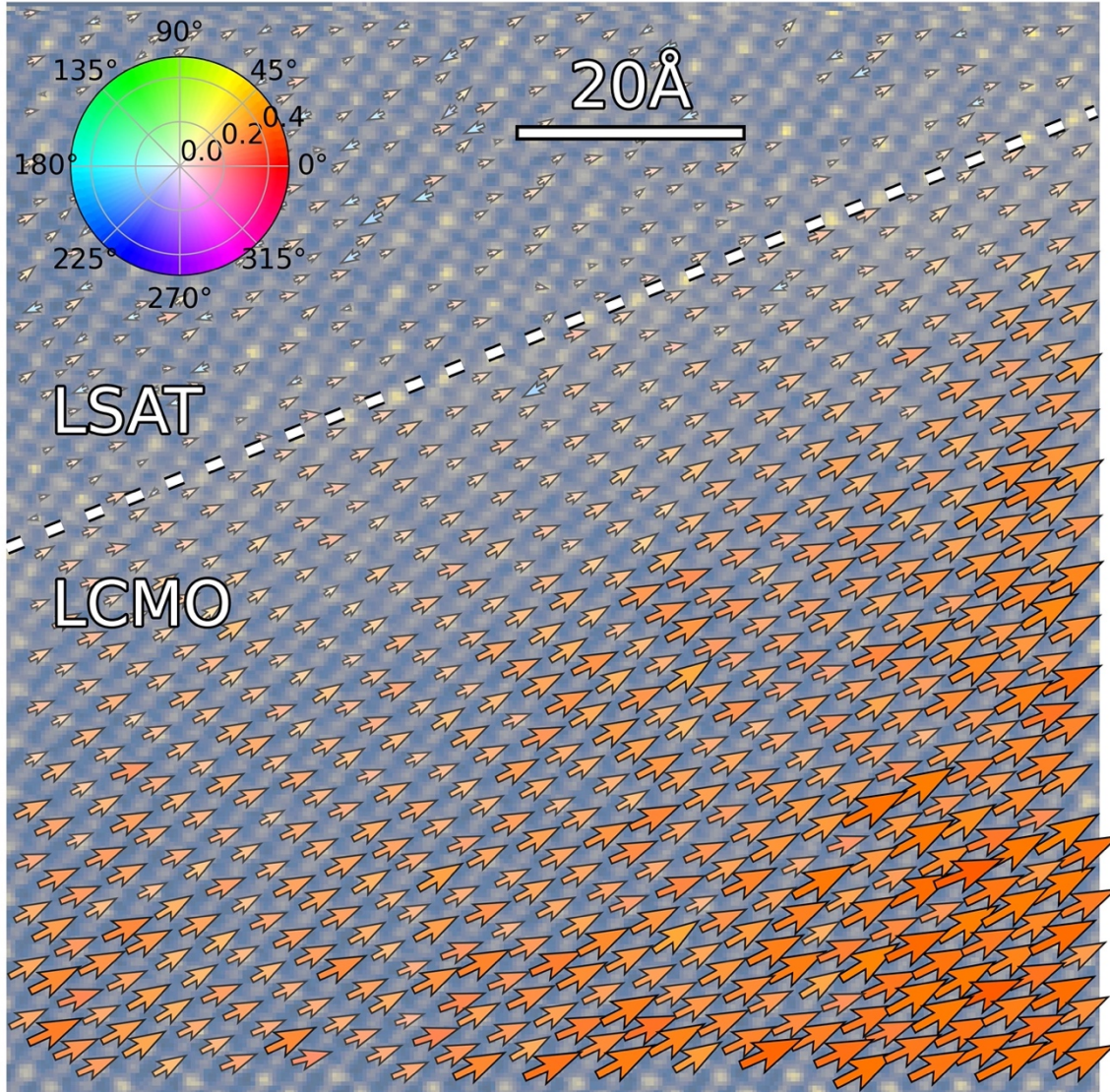


Figure 4: Atomic resolution 3D imaging of a LCMO/LSAT interface area from a 4DSTEM dataset (LSAT substrate above the dotted line, LCMO below). 3D displacement vector orientation and cation modulation strength mapped with atomic resolution with arrows: orientation show the direction in which \mathbf{d} points out of the page, whereas arrow size shows cation modulation strength, and colour correlates to both strength and direction according to the colour wheel (calibrated in Å). This is overlaid on a HAADF image calculated from all electrons scattered above 79 mrad to show the correlation with a standard atomic-resolution projection image.

The arrow map shows no clear modulation in the substrate, as expected, randomly oriented small values (average 9 pm magnitude with an average direction of $59^\circ \pm 72^\circ$ [ACW from horizontal-right]). Throughout the LCMO, however, the modulations all point parallel to the interface towards the top right. The strength of this modulation is very weak for the first few unit cells above the interface (average 16 pm, $28^\circ \pm 23^\circ$ in first 2 nm) but then gradually increases with distance from that interface (average 42 pm, $26^\circ \pm 3^\circ$ > 6 nm from interface). This is in accordance with previous measurements from this very film^{11,26}, as well as many previous studies showing that strain and properties in thin perovskite films often

increase to the full value in a few nm from the substrate, as a result of the constraining effects of the interface^{18,19,29,30}. Previous work on the LCMO growth concentrated on the effect of using a {111} growth surface to promote the octahedral tilting necessary to create a periodic modulation of B-site size which then results in ordering of Co and Mn, and thereby strong antiferromagnetic ordering with a strong magnetic moment²⁶. However, the present result indicates that this growth surface promotes in-plane A-site modulation resulting in the **d**-vector, and consequently the **b**-axis of the crystal structure, preferentially lying in-plane. The same trend has been seen in seven atomic-resolution datasets from different areas of the same film. A similar approach has also been applied to a dataset from the film recorded over a much larger image area (not at atomic resolution) and the same still holds true (although absolute mapping of the sense of the **b**-axis inclination is then not possible because of not having both the atomic resolution imaging of column positions and the A_1 parameter peak positions); this is shown in the supplemental information (Figure S4). As has previously been concluded, octahedral tilting and A-site modulation are all connected in complex oxides like this^{19,26}, and promoting a particular A-site modulation direction appears to be a powerful way to control the octahedral tilting.

Atomic resolution mapping gives us new insights into thin film growth

This brings us to the question of why the A-site modulation should be preferentially in-plane. Generally, domain orientations in perovskite thin films have mainly been found to be determined by strain minimisation (for instance Lebedev *et al.*^[31], MacLaren *et al.*^[32]). As it turns out, this may be also true here. This is summarised visually in **Figure 5**. LSAT should have a relatively short pseudocubic $\langle 110 \rangle$ vector of length 5.473Å. The **b** axis of LCMO should be 5.483Å in length (so 0.18% compressive strain), $[11\bar{1}]_{\text{LCMO}}/[1\bar{1}\bar{1}]_{\text{LCMO}}$ should be 5.497Å (0.46% compressive strain) and $[111]_{\text{LCMO}}/[1\bar{1}\bar{1}]_{\text{LCMO}}$ should be 5.501Å (0.52% compressive strain). So, all of these could be relatively low strain if laying in-plane. In contrast, the **a**-axis of LCMO should be 5.525Å, which is a significantly higher strain of 0.94%. So, the most energetically favourable configurations will be with **b** and two $\langle 111 \rangle_{\text{LCMO}} / \langle 1\bar{1}\bar{1} \rangle_{\text{LCMO}}$ axes in plane on the (111) surface of the LSAT. This results in a slightly larger spacing normal to the interface (2.25 Å unstrained) than it would for **a**-axis in-plane (2.24Å unstrained) (ignoring any Poisson's ratio effects which would probably increase this further^[29]), which probably creates more space to incorporate ordered layers of larger Co atoms. This may well be the reason for better Mn/Co ordering on (111) LSAT than growing on (111) SrTiO₃^[26] (which has a larger lattice parameter that will probably not favour the same domain orientations). And better Mn/Co ordering gives better ferrielectric ordering and a stronger magnetic moment, and thus better properties. This work therefore provides a method for understanding the structural origins of these improved properties.

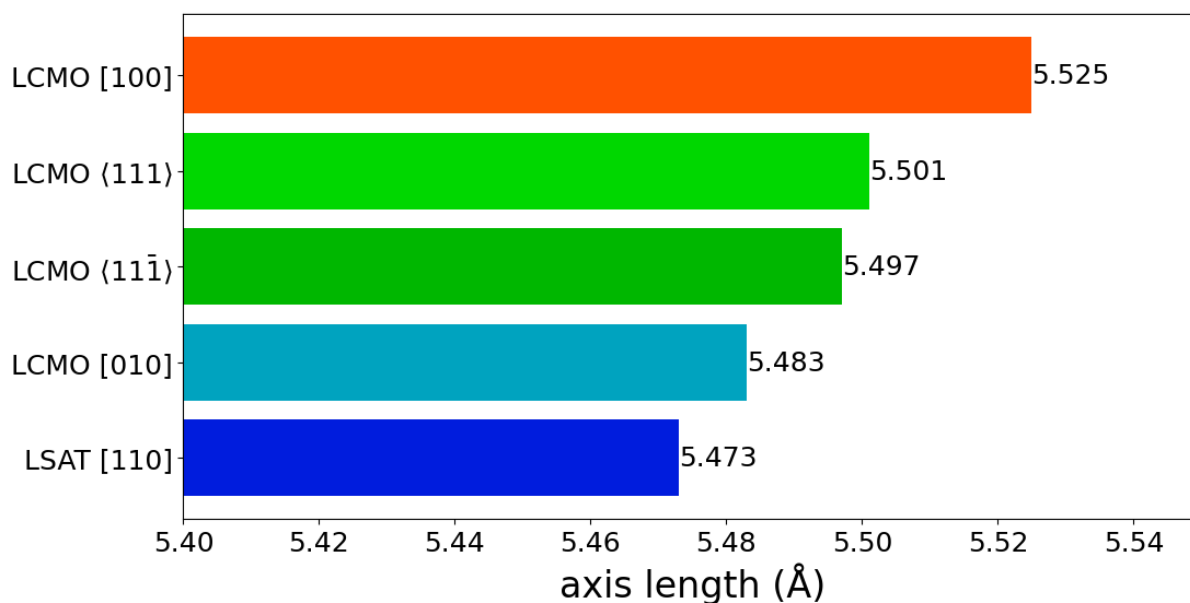


Figure 5: Axes lengths for different directions in LCMO equivalent to cubic $\langle 110 \rangle$ directions, and a comparison to the [110] length in the LSAT substrate.

One thing that is clear is that this level of detail about domain structures and how they relate to distinct crystallographic axes in characterisation techniques was not seen in any characterisation techniques used previously. Perhaps with a lot of sample tilting in the TEM goniometer, evidence could be found for some domains with **b**-directions in plane using TEM nanobeam diffraction (this would require getting [010] on-axis, and since this would require tilts of $>60^\circ$ for some domains, is not feasible for all or even most domains). Similarly, some differences in $\langle 110 \rangle_{\text{pseudocubic}}$ lattice parameters in-plane and at a 54° angle to the interface plane out could maybe be determined by very careful thin film X-ray diffraction. But this method of fitting the high angle electron scattering provides much more straightforward and spatially resolved information than any prior method.

Wider significance of this work – atomic resolution crystallography using STEM

More generally, this work shows a way forward for mapping 3D crystallography with atomic column resolution. Any feature of a diffraction pattern that varies across a unit cell as a function of radial or azimuthal angle could be extracted by similar approaches to these of fitting data with appropriate mathematical functions, and if applied to 4DSTEM data taken at suitable spatial resolution, could be investigated at the atomic scale. This could include any modulation or chiral displacement of atoms along a column. Of course, each case would need validation by simulation to enable the interpretation of the atomic resolution diffraction signals, in a similar way to in this work. This will be especially powerful in observing the variation of crystallography at the nano- or atomic-scale (i.e. basically inaccessible to traditional bulk diffraction techniques) in the vicinity of internal interfaces and defects in materials and heterostructures. It would also be incredibly powerful at elucidating the details of structure and composition on a column resolved scale in larger unit cell complex oxides and other complex compounds, where the structure solution from single

crystal X-ray or neutron methods is ambiguous and somewhat depends on starting guesses for the occupancy of different sites (e.g. the work of Azough *et al.*²³).

Conclusions

In summary, we show that it is possible to directly map the azimuthal variation in intensity of a First Order Laue Zone ring in electron diffraction of a double perovskite in atomic resolution 4DSTEM imaging. This can be simply parametrised as the amplitudes and peak angles for 2-fold and 1-fold functions of azimuthal angle. The resulting parameter maps reveal a wealth of atomic resolution detail when applied to imaging of a $\text{La}_2\text{CoMnO}_6$ (LCMO) film along a $\langle 111 \rangle_{\text{monoclinic}} / \langle 110 \rangle_{\text{cubic}}$ direction. With the aid of theoretical simulations, this allows the unambiguous mapping of atomic displacements in three dimensions from a single scan. This showed the expected suppression of displacement close to the substrate interface, but a rapid rise to close to the bulk value in about 6 nm. However, this also showed a novel insight, specifically that the **b**-axis sits preferentially in the plane of the interface. Further analysis showed that this likely occurred for strain minimisation reasons, but would have been hard to see by techniques available prior to this work (including prior techniques in STEM imaging). More generally, this work demonstrates a new approach to atomic resolution imaging in the electron microscope that is not simply projection imaging, but explicit works on mapping of 3D crystallographic parameters in atomic resolution images from fitting diffraction features in atomic resolution 4DSTEM datasets. It is anticipated that this broad concept will have a major impact on the atomic scale understanding of materials and nanostructures in the future, especially in systems where the crystallography is all tied to a single crystal orientation of some fundamental lattice such as epitaxial systems, domain structures, displacive transformations, and order-disorder transitions.

Methods

Sample preparation and scanning transmission electron microscopy

The $\text{La}_2\text{CoMnO}_6$ sample was grown by pulsed laser deposition on a (111) substrate of LSAT at a substrate temperature of 710°C using a repetition rate of 1Hz and a fluence of 1.5 Jcm^{-2} under 0.15 mbar flowing O_2 , followed by annealing at 700°C for 30 min under 500 mbar O_2 , and finally slow cooling to room temperature. A sample was prepared for STEM using a standard FIB liftout procedure. Further details are given in Kleibeuker *et al.*²⁶.

Scanning transmission electron microscope datasets were acquired using a JEOL ARM300F at the ePSIC facility at Diamond Light Source operated at 200 kV with the diffraction patterns acquired using a 2x2 tiled Medipix detector providing 515x515 pixel images. The convergence angle of the probe was 20 mrad and the camera length was set to allow angles of up to about 97 mrad to reach the detector (centre to middle of edge), and a step size of $\sim 0.5 \text{ \AA}$ was used to collect the dataset shown.

Data handling and initial processing (polar transform and fitting)

Conversion of the raw data to hdf5 was performed on site at Diamond Light Source, and all calculations were done on datasets where the diffraction dimension had been binned by a factor of 4 prior to further processing, since this both reduced memory requirements and

increased processing speed, with no noticeable loss of any information in the results of the analysis. The centre of the FOLZ ring in the dataset was determined by overlaying a circle on the data and shifting this until it best matched the ring (as the centre-of-mass of the diffraction pattern, dominated by low angle scattering, can differ slightly from the centre of the FOLZ, if there is slight sample mistilt). This was then followed by performing the polar transform and testing if the Laue Zone ring is a straight line after transform.

Polar transform over entire 4DSTEM datasets was performed using home-built code (provided in the data deposit, alongside all other code pieces and raw data used in this work) based on the earlier implementation of Barthel in *emilys*, using the same maths, but optimised for fast calculation of an entire dataset. The relevant feature of the FOLZ ring was identified (the outer part of the split ring¹⁸) corresponding most strongly to the La-O columns and integrated to a 1D line plot of intensity as a function of azimuthal angle. This was then fitted to Equation (1) using *scipy.optimize.curve_fit* using a simple iterative function that fits each pixel in the real space scan in turn.

Multislice simulation of 4DSTEM datasets and matching to experiment

Simulated 4DSTEM datasets were calculated from the structure of Bull *et al.*²⁴ using a multislice approach with the Dr Probe package³³, for a sample thickness of 53 nm. For the multislice simulations of the structure in [111] orientation, a supercell of size $a = 3.84731$ nm, $b = 3.89183$ nm, and $c = 1.10062$ nm was set up and partitioned into 8 slices along the c direction, i.e. the direction parallel to that of the incident electron probe. The slices were set such that each contains one atomic plane. Projected scattering potentials were prepared on a grid of 720×720 pixels for the (a,b) planes. For simulating the effects of thermal diffuse scattering within the quantum excitation of phonons model³⁴, 100 atomic configurations were prepared for each slice. High angle diffraction patterns were calculated for a pixelated detector of 384×384 pixels placed in the diffraction plane (far field) with a pixel step of 0.25 mrad, assuming the experimental STEM parameters noted above and for every point in a scan at a similar pixel sampling to the experimental data. This simulated 4DSTEM dataset was processed in the same way as the experimental data, and when comparing to experimental datasets averaged from many unit cells, it should be noted that the theoretical simulation is also the average of 100 different simulations.

The experimental dataset for comparison was interpolated by a factor of 4 using *scipy.ndimage.zoom* and then 121 unit cell origins were found on La-O columns using *atomap*³⁵ and used to determine image patches for superposition and summation – the interpolation meant that the results were not smeared by the origins varying at the subpixel level.

Mapping of displacement vectors in 3D

To convert a map of fit parameters to a map of antiparallel La atom displacement orientations firstly needs sets of peak positions to be determined with *Atomap*³⁵: La-column HAADF peaks, and the peak positions in the A_1 map (being easier to quantify reliably than the trough positions). These are then sorted by coordinates and nearest-neighbour A_1 -site peaks are associated with each La column peak (i.e. HAADF peak) in sorted lists. These are then used to look up the ϕ_2 angle for each column (at the positions of the A_1 -peaks), and

give the sense of the **d**-axis. The strength of the modulation is determined from the A_2 values at the peaks and troughs of A_1 . The resulting data can then be plotted as a map of displacement direction, **d**, (pretty close to **b**), and atom off-centre shift, normalised to the maximum value observed previously by structure refinement²⁴. This plot can be then displayed using a range of representations (e.g. arrow or “quiver” plot, colormap).

Acknowledgements

This work would never have been possible without the EPSRC funding of the grant “Fast Pixel Detectors: a paradigm shift in STEM imaging” (EP/M009963/1), which started the work that led to this and funded the computer server used in the calculations. We thank Diamond Light Source for access and support in use of the electron Physical Science Imaging Centre (Instrument E02 and proposal number EM16952) that contributed to the results presented here. The films were grown with the support of the European Research Council (ERC) (Advanced Investigator grant ERC-2009-AdG-247276-NOVOX), the EPSRC (Equipment Account Grant EP/K035282/1) and the Isaac Newton Trust (Minute 13.38(k)). IM is grateful to Prof Peter D. Nellist for helpful discussions as part of the EPSRC grant named above and to the late Prof John C.H. Spence for helpful discussions and encouragement to pursue work on HOLZ in 4DSTEM.

Author Credit Statement

Ian Maclaren came up with original concept for this work, oversaw all aspects and led the writing of this paper. Aurys Silinga developed the azimuthal intensity fitting of HOLZ rings. Juri Barthel performed the simulations of 4DSTEM datasets. Josee Kleibecker grew the films under the direction of Judith MacManus-Driscoll. Christopher Allen performed the microscopy at the ePSIC facility, with input and oversight from Angus Kirkland. All authors contributed to the writing of the final paper.

References

- 1 Batson, P. E., Dellby, N. & Krivanek, O. L. Sub-angstrom resolution using aberration corrected electron optics. *Nature* **418**, 617-620, (2002).
- 2 Haider, M. *et al.* Electron microscopy image enhanced. *Nature* **392**, 768-769, (1998).
- 3 Nellist, P. D. *et al.* Direct sub-angstrom imaging of a crystal lattice. *Science* **305**, 1741-1741, (2004).
- 4 MacLaren, I. & Ramasse, Q. M. Aberration-corrected scanning transmission electron microscopy for atomic-resolution studies of functional oxides. *Int. Mater. Rev.* **59**, 115-131, (2014).
- 5 Pennycook, S. J. & Varela, M. New views of materials through aberration-corrected scanning transmission electron microscopy. *J. Electron Microsc.* **60**, S213-S223, (2011).
- 6 MacLaren, I. & Richter, G. Structure and possible origins of stacking faults in gamma-yttrium disilicate. *Philos. Mag.* **89**, 169-181, (2009).
- 7 MacLaren, I. *et al.* Novel Nanorod Precipitate Formation in Neodymium and Titanium Codoped Bismuth Ferrite. *Adv. Func. Mater.* **23**, 683-689, (2013).
- 8 MacLaren, I. *et al.* Local stabilisation of polar order at charged antiphase boundaries in antiferroelectric $(\text{Bi}_{0.85}\text{Nd}_{0.15})(\text{Ti}_{0.1}\text{Fe}_{0.9})\text{O}_3$. *APL Mater.* **1**, (2013).
- 9 Chen, C.-C. *et al.* Three-dimensional imaging of dislocations in a nanoparticle at atomic resolution. *Nature* **496**, 74-77, (2013).
- 10 Ophus, C. Four-Dimensional Scanning Transmission Electron Microscopy (4D-STEM): From Scanning Nanodiffraction to Ptychography and Beyond. *Microsc. Microanal.* **25**, 563-582, (2019).
- 11 MacLaren, I., Macgregor, T. A., Allen, C. S. & Kirkland, A. I. Detectors—The ongoing revolution in scanning transmission electron microscopy and why this important to material characterization. *APL Mater.* **8**, 110901, (2020).
- 12 Crewe, A. V., Wall, J. & Langmore, J. Visibility of Single Atoms. *Science* **168**, 1338-1340, (1970).
- 13 Pennycook, S. J. & Jesson, D. E. High-Resolution Z-Contrast Imaging of Crystals. *Ultramicroscopy* **37**, 14-38, (1991).
- 14 Findlay, S. D. *et al.* Dynamics of annular bright field imaging in scanning transmission electron microscopy. *Ultramicroscopy* **110**, 903-923, (2010).
- 15 LeBeau, J. M., D'Alfonso, A. J., Findlay, S. D., Stemmer, S. & Allen, L. J. Quantitative comparisons of contrast in experimental and simulated bright-field scanning transmission electron microscopy images. *Phys. Rev. B* **80**, (2009).

- 16 Chapman, J. N., McFadyen, I. R. & McVitie, S. Modified differential phase-contrast lorentz microscopy for improved imaging of magnetic-structures. *IEEE Trans. Magn.* **26**, 1506-1511, (1990).
- 17 Shibata, N. *et al.* Differential phase-contrast microscopy at atomic resolution. *Nat. Phys.* **8**, 611-615, (2012).
- 18 Nord, M. *et al.* Atomic resolution HOLZ-STEM imaging of atom position modulation in oxide heterostructures. *Ultramicroscopy* **226**, 113296, (2021).
- 19 Nord, M. *et al.* Three-dimensional subnanoscale imaging of unit cell doubling due to octahedral tilting and cation modulation in strained perovskite thin films. *Phys. Rev. Mater.* **3**, 063605, (2019).
- 20 Huang, F. T. *et al.* Scanning Transmission Electron Microscopy Using Selective High-Order Laue Zones: Three-Dimensional Atomic Ordering in Sodium Cobaltate. *Phys. Rev. Lett.* **105**, 125502, (2010).
- 21 Woodward, D. I. & Reaney, I. M. Electron diffraction of tilted perovskites. *Acta Crystallogr. Sect. B-Struct. Commun.* **61**, 387-399, (2005).
- 22 Glazer, A. M. Classification of Tilted Octahedra in Perovskites. *Acta Crystallogr. Sect. B-Struct. Commun.* **B 28**, 3384-3392, (1972).
- 23 Azough, F. *et al.* Tungsten Bronze Barium Neodymium Titanate ($\text{Ba}_{6-3n}\text{Nd}_{8+2n}\text{Ti}_{18}\text{O}_{54}$): An Intrinsic Nanostructured Material and Its Defect Distribution. *Inorg. Chem.* **55**, 3338-3350, (2016).
- 24 Bull, C. L., Playford, H. Y., Knight, K. S., Stenning, G. B. G. & Tucker, M. G. Magnetic and structural phase diagram of the solid solution $\text{LaCo}_x\text{Mn}_{1-x}\text{O}_3$. *Phys. Rev. B* **94**, 014102, (2016).
- 25 Silinga, A., Allen, C. S., Barthel, J., Ophus, C. & MacLaren, I. Measurement of Atomic Modulation Direction Using the Azimuthal Variation of First-Order Laue Zone Electron Diffraction. *Microsc. Microanal.*, ozad089 (early view), (2023).
- 26 Kleibeuker, J. E. *et al.* Route to achieving perfect B-site ordering in double perovskite thin films. *NPG Asia Materials* **9**, (2017).
- 27 Goodman, P. & Moodie, A. F. Numerical evaluations of N-beam wave functions in electron scattering by the multi-slice method. *Acta Crystallogr A* **30**, 280-290, (1974).
- 28 Cowley, J. M. & Moodie, A. F. The scattering of electrons by atoms and crystals. I. A new theoretical approach. *Acta Crystallographica* **10**, 609-619, (1957).
- 29 MacLaren, I., Wang, Z. L., Wang, H. S. & Li, Q. Strain-induced crystal structure change in ultrathin films of $\text{Pr}_{0.7}\text{Sr}_{0.3}\text{MnO}_3$. *Appl. Phys. Lett.* **80**, 1406-1408, (2002).

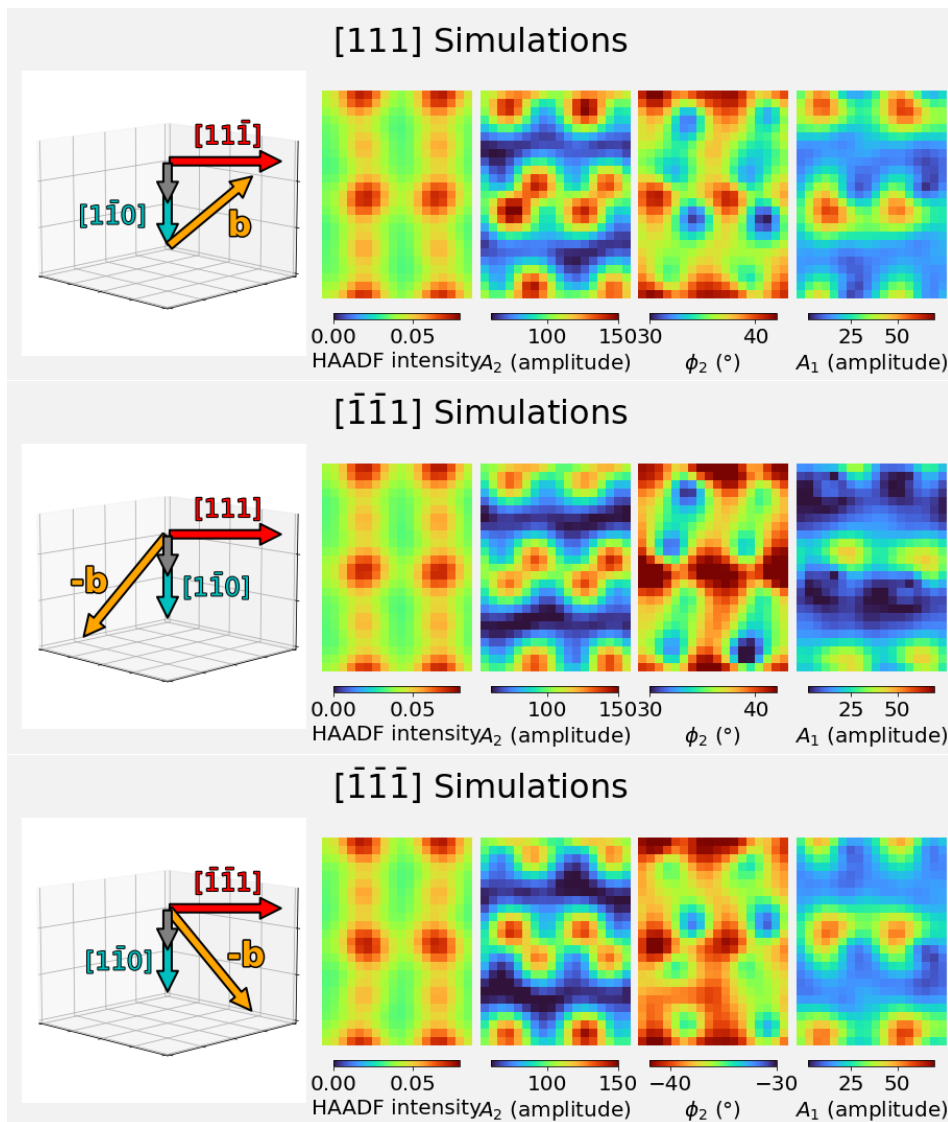
- 30 Borisevich, A. Y. *et al.* Suppression of Octahedral Tilts and Associated Changes in Electronic Properties at Epitaxial Oxide Heterostructure Interfaces. *Phys. Rev. Lett.* **105**, (2010).
- 31 Lebedev, O. I. *et al.* Structure and microstructure of $\text{La}_{1-x}\text{Sr}_x\text{MnO}_3$ ($x \approx 0.16$) films grown on a $\text{SrTiO}_3(110)$ substrate. *Philos. Mag. A* **81**, 2865-2884, (2001).
- 32 MacLaren, I., Wang, Z. L., Wang, H. S. & Li, Q. The effects of film-substrate mismatch on $\text{Pr}_{0.7}\text{Ca}_{0.3}\text{MnO}_3$ thin films. *Philos. Mag. A* **82**, 1405-1417, (2002).
- 33 Barthel, J. Dr. Probe: A software for high-resolution STEM image simulation. *Ultramicroscopy* **193**, 1-11, (2018).
- 34 Forbes, B. D., Martin, A. V., Findlay, S. D., D'Alfonso, A. J. & Allen, L. J. Quantum mechanical model for phonon excitation in electron diffraction and imaging using a Born-Oppenheimer approximation. *Phys. Rev. B* **82**, 104103, (2010).
- 35 Nord, M., Vullum, P. E., MacLaren, I., Tybell, T. & Holmestad, R. Atomap: a new software tool for the automated analysis of atomic resolution images using two-dimensional Gaussian fitting. *Advanced Structural and Chemical Imaging* **3**, 9, (2017).

Atomic resolution imaging of 3D crystallography in the scanning transmission electron microscope

Ian MacLaren¹, Aurys Silinga¹, Juri Barthel², Josee Kleibeuker^{3,4}, Judith L MacManus-Driscoll³, Christopher S Allen^{5,6}, Angus I Kirkland^{5,6}

1. School of Physics and Astronomy, University of Glasgow, Glasgow G12 8QQ, UK
2. Ernst Ruska-Centre (ER-C 2), Forschungszentrum Jülich GmbH, 52425 Jülich, Germany
3. Department of Materials Science & Metallurgy, University of Cambridge, 27 Charles Babbage Road, Cambridge CB3 0FS, UK
4. DEMCON high tech systems Eindhoven BV, Kanaaldijk 29, 5683 CR Best, The Netherlands
5. electron Physical Science Imaging Centre, Diamond Light Source Ltd., OX11 0DE, UK
6. Department of Materials, University of Oxford, Parks Road, Oxford OX1 3PH, UK

Demonstration that this mapping works consistently for $\langle 111 \rangle_{\text{monoclinic}}$ directions



Figs S1-S3: Fitting results for 4DSTEM simulations for three beam directions representative of all $\langle 111 \rangle_{\text{monoclinic}}$ directions. Detailed commentary given in the text.

Simulated 4DSTEM datasets were calculated for several different $\langle 111 \rangle_{\text{monoclinic}}$ directions corresponding to the main distinct ones in this monoclinic structure. It is in a standard setting with $\beta \neq 90^\circ$, thus, there is basically no difference between $[uvw]$ and $[u\bar{v}w]$. There is, however, a significant difference between $[uvw]$ and $[uv\bar{w}]$ because the **a** and **c** axes are not orthogonal. Thus, $[111]$ and $[\bar{1}\bar{1}1]$ represent the two distinct types of $\langle 111 \rangle_{\text{monoclinic}}$ directions. Including $[\bar{1}\bar{1}\bar{1}]$ demonstrates the effect looking along a direction in the opposite sense.

The first main point to notice is that very similar features come out in all maps. Note, the ϕ_2 is measured clockwise from the vertical direction in all maps. This is reversed (as is the colour map) in Fig S3 where the “dumbbell” structure is pointing anticlockwise from vertical. So this parameter always tracks with the appearance of the maps. The really important point is that the direction in which the **b** axis (or **-b**) direction points up out of the sample plane is always in the direction from the A_1 peaks to the HAADF peaks.

There is a minor difference between $[111]$ and $[\bar{1}\bar{1}1]$ analyses in that the variations in the ϕ_2 and A_1 maps are slightly stronger for the latter, presumably slight differences in the angle of the displacement vector, **d**, to these directions causes a stronger effect in one case than the other.

A note on the 3D vector plots – these are done to roughly indicate the 3D direction of the vectors (although are done using a pseudocubic approximation of the axis lengths). To allow visibility of the grey Beam direction vector, these are tilted down by 11° so are not quite along the same direction as the Beam direction for the 4DSTEM datasets but are there to show the relative orientation of the key vectors in each image. In each case, the correct indices for the horizontal right direction (in monoclinic vectors) are given in red, and those for the vertical down direction in cyan. Beam directions are calculated with the normal convention for electron microscopy as being vertical upwards from the page, antiparallel to the direction of electron motion and parallel to the direction of current flow.

Large area mapping of same film (not at atomic resolution)

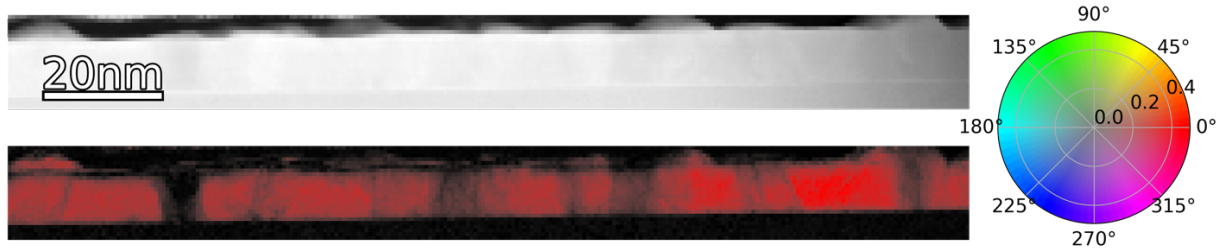


Figure S4: Upper: HAADF image of the large area of this film with carbon to the top, film in the middle, and LSAT substrate at the bottom. Lower: large area mapping of the direction of the **d**-axis for this film of LCMO on LSAT. All colour mapping of directions referenced to the image axes. **d** consistently lies close to in-plane suggesting that the **b** axis is in-plane for much of the film.

Applying the method of this paper to a large area 4DSTEM dataset from the same film results in the following map in Figure S4. This shows that almost all areas have **d** laying in-plane at some angle to the specimen plane, suggesting the **b** lays preferentially in-plane. Some areas are dark in this map, which indicates regions where the inner FOLZ disappears and must correspond to other crystal orientations (separate evidence from low convergence angle nanobeam electron diffraction suggests these are $[010]$ oriented domains). There is no evidence in the whole dataset for any area where the **b**-axis does not lie in the film plane.